

Resolving electrical conductivities from collisionally damped plasmons in isochorically heated warm dense aluminum

P. Sperling,¹ L. B. Fletcher,¹ H.-K. Chung,² E. J. Gamboa,¹ H. J. Lee,¹ Y. Omarbakiyeva,^{3,4}
H. Reinholz,^{4,5} G. Röpke,⁴ S. Rosmej,⁴ U. Zastrau,⁶ and S. H. Glenzer¹

¹*SLAC National Accelerator Laboratory, 2575 Sand Hill Road, MS 72 Menlo Park, CA 94025 USA*

²*Nuclear Data Section, Division of Physical and Chemical Sciences,
International Atomic Energy Agency, A-1400 Vienna, Austria*

³*International IT University, 050040, Almaty, Kazakhstan*

⁴*Institut für Physik, Universität Rostock, 18051 Rostock, Germany*

⁵*University of Western Australia, WA 6009 Crawley, Australia*

⁶*European XFEL, Albert-Einstein-Ring 19, 22761 Hamburg, Germany*

(Dated: March 22, 2016)

We measure the highly-resolved inelastic x-ray scattering spectrum of isochorically ultrafast heated aluminum. In the x-ray forward scattering spectra the electron temperature could be measured from the down- and upshifted plasmon, where the electron density of $n_e = 1.8 \times 10^{23} \text{ cm}^{-3}$ is known *a priori*. We have studied the plasmon damping by applying electron-particle collision models beyond the Born approximation determining the electrical conductivity of warm dense aluminum.

PACS numbers: 52.25.Os, 52.35.Fp, 52.50.Jm, 78.70.Ck

I. INTRODUCTION

Warm dense matter (WDM) [1, 2] is characterized by densities of solid density up to compressed matter and temperatures of 1 eV to several 10 eV. Occurring in planets and stars, WDM is relevant for astrophysics to model the interior structure of such objects [3–5]. As transient state of hot dense matter during the laser compression of thermonuclear fuel capsules, WDM is also important for the understanding of inertial confinement fusion (ICF) experiments [6, 7].

In particular, the knowledge of electrical conductivities in the WDM region is of paramount interest to model, e.g., the magnetic field generation in the interior of planets and stars [8, 9]. These fields are induced by WDM fluid streams composed of metals in case of rocky planets [10, 11] and metallic hydrogen in case of Jovian planets [12, 13]. Their magnetic fields are strongly dependent on the electrical conductivity of these streams [14]. Such conductivities are also relevant to model ICF experiments. Here, Rayleigh-Taylor instability growth prevent an efficient fusion process, which is dependent on the electrical conductivity in the WDM region [15]. Therefore, the knowledge of such conductivities is required to model the assembly of thermonuclear fuel capsules for the ICF.

Previous measurements of the electrical conductivity in warm dense matter [16–22] exist, but show order of magnitude discrepancies to theoretical predictions [16, 23, 24]. Due to the lack of accurate plasma characterization techniques the validation of such predictions is challenging. Therefore, widely used theoretical models [25–27] and simulations [28–30] as well as predictions of non-Drude like behaviors in metals in the WDM region [31, 32] await experimental testing.

With the advent of the Linac Coherent Light Source (LCLS) [33, 34] a brilliant x-ray source becomes avail-

able, that allows the investigation of microscopic matter properties. For instance, the LCLS enables with its bandwidth of 10^{-4} and an unprecedented small signal-to-noise ratio the study of electrical conductivities via inelastic x-ray Thomson scattering [35]. X-ray Thomson scattering as a versatile tool to diagnose WDM [36] was developed during the last decades [35, 37–42] to allow an accurate determination of electron density and temperature [36]. Together with this accurate WDM characterization [37], the validation of existing models and simulations of the electrical conductivity became recently available.

In this work we discuss the experimental findings of the electrical conductivity and their comparison with existing theoretical models [35]. First, we present the experimental setup in Sec. II. After, we discuss the LCLS heating process and show simulations that predict electron density and temperature in the experiment. In Sec. IV, we present our measured scattering signals and compare with our calculations. Furthermore, the determination of the experimental electron temperature and the extraction of the dynamical collision frequency from the measured scattering signal is described. In Sec. V we extract the ac and dc conductivity from the data, that allow us to validate different models of the dc conductivity in the liquid and plasma phase of aluminum.

II. EXPERIMENTAL SETUP

In order to allow an isochorical and homogeneous heating of the aluminum target, the LCLS [33] has been operated at $E = 7980 \text{ eV}$ photon energy. The x-ray beam delivers $\approx 7 \times 10^{10}$ photons within 25 fs pulse length (FWHM) (see Fig. 2) on target. The focal spot size of 1 and 10 μm , realized by a compound beryllium refractive lens [43], and the pulse energy of 0.1 mJ provide intensities of $\approx 10^{17} \text{ W/cm}^2$ and $\approx 10^{15} \text{ W/cm}^2$, respectively,

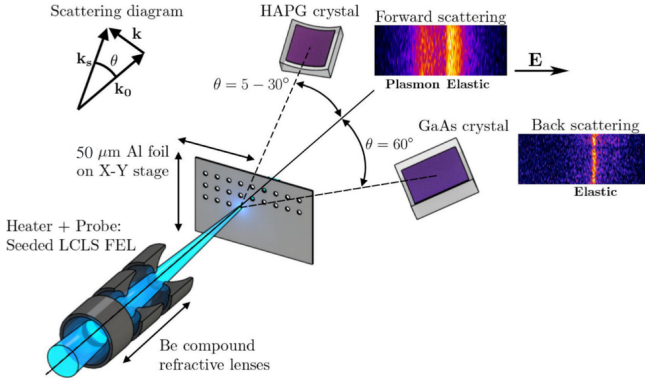


FIG. 1. Schematic of the experimental setup and raw data (figure from [35]). The $50\ \mu\text{m}$ thick aluminum foil is isochorically heated by 7980 eV LCLS photons. For each shot, the photon scattering is observed via two detectors to monitor the source function.

which allow temperature dependent measurements.

As target we use solid aluminum foils with a mass density of $2.7\ \text{g/cm}^3$. To isochorically heat aluminum by photoabsorption, the foil thickness of $50\ \mu\text{m}$ matches the attenuation length. For each shot, an unperturbed aluminum target is provided by a X-Y stage. The target is heated and probed simultaneously by the LCLS [44].

The experiment measures the spectral and angular resolved x-ray scattering. We apply the LCLS in seeded beam mode to avoid a distortion of the plasmon spectra with spectral noise from x-ray amplification. The scattered photons (as illustrated in Fig. 1) were measured in forward direction at $\theta = 18^\circ$ ($k = 1.26\ \text{\AA}^{-1}$) and $\theta = 24^\circ$ ($k = 1.68\ \text{\AA}^{-1}$) by a Highly Annealed Pyrolytic Graphite (HAPG) crystal in a von Hámós configuration [45]. In addition, scattered photons are collected at an angle of $\theta = 60^\circ$ ($k = 4.04\ \text{\AA}^{-1}$) by a GaAs crystal [46]. The comparison of both spectrometer signals allows an accurate monitoring of the source function for each shot (shown later). An extremely small angle uncertainty of $\delta\theta = 0.3^\circ$ ($\delta k = 0.02\ \text{\AA}^{-1}$) is ensured by a small source size and focusing of the seeded LCLS [47]. In addition, the LCLS provide excellent statistics by repetition rates of 120 Hz and small signal-to-noise ratio and spectral resolution by a bandwidth of $\Delta E/E \approx 0.25\%$.

III. X-RAY HEATING OF THE TARGET

We simultaneously heat and probe the aluminum target with the LCLS beam. Its 7×10^{10} photons with an energy of 7980 eV heat the target isochorically and homogeneously via photoabsorption [35, 38, 48]. LCLS photons transfer its energy by photoionisation to the target, where electrons from the valence and conduction band of aluminum are excited to higher electronic energy states. Subsequent relaxation effects as Auger decay and collisions form a local thermal equilibrium.

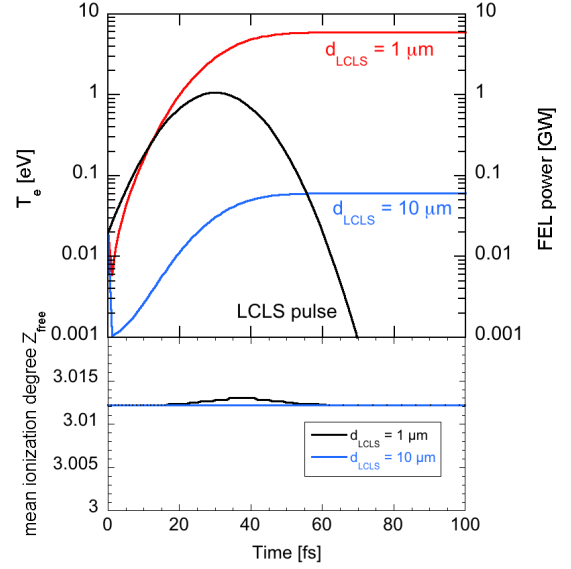


FIG. 2. Idealized Gauss-shaped LCLS pulse and temporal evolution of the electron temperature (upper panel) and mean ionization degree (lower panel) for different LCLS focal spot sizes. The calculations are performed by the code SCFLY [49].

A. Photoionization

The electron temperature and mean ionization degree of the laser-heated aluminum target are predicted by the code SCFLY [49]. The electron density is determined by solving a set of rate equations using collisional-radiative rates. The collisional rates describe excitation, ionization and electron capture whereas the radiative rates characterize spontaneous emission and radiative recombination. In addition, autoionization rates are included. Within the code, ionization potential depression is taken into account by the model of Stewart and Pyatt [50]. The electron temperature is calculated via the absorbed LCLS energy for each time step, where a instantaneous relaxation, e.g., via Auger decay and collisions, is assumed, so that a local thermal equilibrium of the electronic subsystem is formed instantaneously [51]. Therefore, a possible non-equilibrium of the electronic subsystem in the aluminum target can not be described by SCFLY. In addition, the ion temperature can not be inferred by the SCFLY simulations, which influences the ionic structure correlations and thus the electrical conductivity. For predictions of non-equilibrium electron distributions other calculations have to be applied [52]. Instead, we will determine a characteristic temperature from the measured scattering spectra.

Fig. 2 shows the assumed Gauss-shaped LCLS pulse and the temporal evolution of the electron temperature

and mean ionization degree for different LCLS focal spot sizes. For our experimental conditions, SCFLY predicts final electron temperatures of 6 eV (0.06 eV) for focal spot sizes of 1 μm (10 μm), whereas no significant photoionization is observed indicated by an almost constant ionization degree during the heating process.

IV. X-RAY THOMSON SCATTERING

A. Experimental scattering spectra

The x-ray scattering spectra are measured at angles of $\theta = 18^\circ$, 24° , and 60° and focal spot sizes of 1 and 10 μm . Each spectrum, shown in Fig. 3, is a collection of 2000 shots. The source function was determined by the spectrum collected at an angle of $\theta = 60^\circ$ for each shot. In comparison to the forward scattering spectrum, which shows collective scattering on plasmons [36], the spectrum collected at $\theta = 60^\circ$ shows the non-collective Compton scattering. This scattering is well investigated [36] and can be subtracted from the spectrum. The remaining spectrum defines the source function. The deconvolution of the scattering spectra with this source function leads to the deconvolved data.

Fig. 3 shows the experimental and deconvolved scattering spectra together with the corresponding source function. Both experimental spectra show a dominant elastic peak at the incident photon energy characterizing the scattering on bound electrons and an inelastic feature downshifted by ≈ 20 eV (≈ 22.5 eV) for scattering angles of 18° (24°). In the deconvolved spectra the elastic peak narrows, but a reproduction of the width of this peak is not possible due to the use of a numerical deconvolution method. After deconvolution, the inelastic downshifted feature narrows and the peak position shifts.

Considering the blue wing of the spectra measured with 1 μm focal spot sizes, a disagreement of the source function and the spectrum indicates an upshifted plasmon. The downshifted (upshifted) inelastic feature defines plasmon excitations (deexcitations) of the delocalized electrons of the aluminum conduction band. The plasmon width defines their lifetime that is affected by electron-particle collisions.

B. Thomson scattering

In order to describe the measured scattering spectra shown in Fig. 3, the theoretical background to calculate such spectra is presented below. The scattered power on N electrons per solid angle $d\Omega$ and frequency interval $d\omega$ is defined by [36]

$$P_S(\mathbf{R}, \omega) d\Omega d\omega = \frac{3P_0 \sigma_T d\Omega}{16\pi^2 A} N S(k, \omega) d\omega |\hat{\mathbf{k}}_S \times (\hat{\mathbf{k}}_S \times \hat{\mathbf{E}}_0)|^2, \quad (1)$$

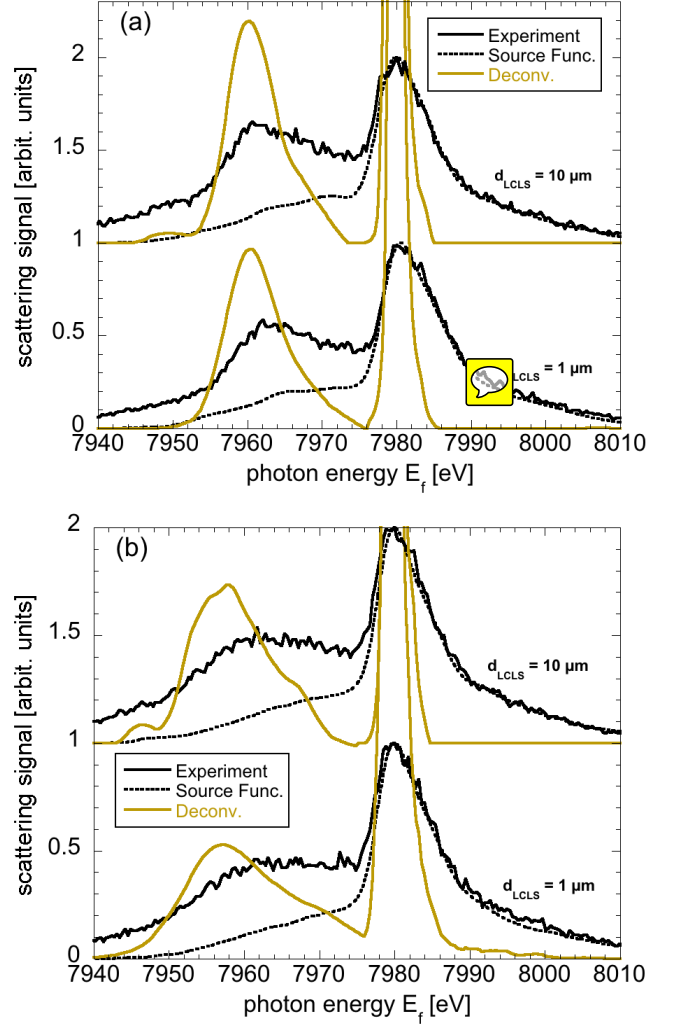


FIG. 3. Measured and deconvolved x-ray scattering spectra and source function as a function of the photon energy for focal spot sizes of 1 and 10 μm (offset by 1 for clarity) and scattering angles of (a) 18° and (b) 24° . The LCLS operates at photon energies of 7980 eV.

and depends on the incident light power P_0 irradiating the plasma area A and the Thomson cross section $\sigma_T = 8\pi r_0^2/3 = 0.665 \times 10^{-24} \text{ cm}^2$, with the classical electron radius $r_0 = 2.8 \times 10^{-15}$. The dipole character of the Thomson scattering is taken into account by the incoming light polarization direction $\hat{\mathbf{E}}_0$ and the unit wave vector $\hat{\mathbf{k}}_S$ of the scattered light. For linearly polarized light we find $|\hat{\mathbf{k}}_S \times (\hat{\mathbf{k}}_S \times \hat{\mathbf{E}}_0)|^2 = (1 - \sin^2 \theta \cos^2 \varphi)$ [53], with the azimuthal φ and polar angle θ . In the experiment, the azimuthal angle is chosen so ($\varphi = 90^\circ$) that the polarization term is unity. In addition, the scattering in a many particle system depends on electron density fluctuations characterized by the dynamic structure factor $S(k, \omega)$. The energy and momentum transfer are given by $\Delta E = \hbar\omega = \hbar(\omega_f - \omega_i)$ and $\hbar\mathbf{k} = \hbar(\mathbf{k}_f - \mathbf{k}_i)$ with the initial and final state of the wavenumber \mathbf{k}_i , \mathbf{k}_f and

frequency ω_i , ω_f .

The dynamic structure factor can be expressed by Chiharas approach [54, 55]

$$S_{ee}(k, \omega) = \underbrace{Z_{\text{free}} S_{ee}^0(k, \omega)}_{\text{free-electron feature}} + \underbrace{|f_i(k) + q(k)|^2 S_{ii}(k, \omega)}_{\text{ion feature}} + \underbrace{Z_c \int_{-\infty}^{\infty} d\omega' S_c(k, \omega) S_s(k, \omega - \omega')}_{\text{bound-free transitions}} \quad (2)$$

and is composed of contributions due to the individual electronic states: the free (free-electron feature, S_{ee}^0) and bound state. After photon scattering, the final state of a bound electron can be a bound (ion-feature, S_{ii}) or free (bound-free transitions, S_c) state. The structure factor of free electrons S_{ee}^0 , ions S_{ii} , and bound-free transitions S_c are weighted by the mean ionization degree Z_{free} , the form factor f_i accounting for core electrons and the screening function q accounting for weakly bound electrons, and the mean number of bound electrons per atom/ion Z_c , respectively. The bound-free transitions has to be convolved with the structure factor S_s representing the motion of the ion.

In this work the photon scattering on free electrons is

studied. Their structure factor can be derived from the fluctuation-dissipation theorem

$$S_{ee}^0(k, \omega) = -\frac{\varepsilon_0 \hbar k^2}{\pi e^2 n_e} \frac{\text{Im } \varepsilon_l^{-1}(k, \omega)}{1 - \exp\left(\frac{-\hbar\omega}{k_B T_e}\right)}. \quad (3)$$

The longitudinal dielectric function for non-interacting plasmas ε_l can be expressed via the Random-Phase-Approximation (RPA) $\varepsilon_l^{\text{RPA}}$. Considering interacting plasmas, electron-ion collisions can be included via the longitudinal dielectric function in Mermin approximation (MA) [56, 57]

$$\varepsilon_l^{\text{M}}(k, \omega, \nu(\omega)) = 1 + \frac{(1 + i\nu(\omega)/\omega)(\varepsilon_l^{\text{RPA}}(k, \omega + i\nu(\omega)) - 1)}{1 + (i\nu(\omega)/\omega)(\varepsilon_l^{\text{RPA}}(k, \omega + i\nu(\omega)) - 1)/(\varepsilon_l^{\text{RPA}}(k, 0) - 1)}, \quad (4)$$

where collisions are taken into account via the dynamical relaxation frequency $\nu(\omega)$, which is complex in general [27, 35]. The real part of the relaxation frequency determines the damping by relaxation processes, e.g, collisions, whereas the imaginary part determines a phase shift between relaxation process and the electrical field. In what follows, we will approximate the relaxation frequency by an electron-particle collision frequency and neglect other relaxing processes.

C. Dynamical collision frequency for Coulomb plasmas

In this section, we will consider dynamical collisions for Coulomb plasmas, where we assume a screened Coulomb potential and neglect ionic structure correlations. The static electron-particle collision frequency is well known for ideal plasmas by the Spitzer expression [26]. In the low density limit, complex dynamical collision frequencies in degenerated and strongly coupled plasmas can be consistently calculated within the generalized linear-response theory [58]. These dynamical collisions can be expressed by a Feynman diagram and is shown in Fig. 4

(a). However this expression can not be calculated exactly and has to be approximated. For instance, collisions in weakly coupled plasmas can be described within the Born approximation, cf. Fig. 4 (b), taking into account weak collisions

$$\nu^{\text{Born}}(\omega) = -i \frac{\varepsilon_0 n_i \Omega_0^2}{6\pi^2 e^2 n_e m_e} \times \int_0^\infty dk k^6 V_{ei}^2(k) S_{ii}(k) \frac{\varepsilon_l^{\text{RPA}}(k, \omega) - \varepsilon_l^{\text{RPA}}(k, 0)}{\omega}. \quad (5)$$

V_{ei} is the electron-ion potential, Ω_0 is the normalization volume, and S_{ii} is the static ionic structure factor.

Within strongly coupled plasmas higher-density effects have to be taken into account, that can be realized via the Gould-DeWitt approach [27]

$$\nu^{\text{GDW}}(\omega) = \nu^{\text{TM}}(\omega) + \nu^{\text{LB}}(\omega) - \nu^{\text{Born}}(\omega), \quad (6)$$

which includes contributions of strong collisions ν^{TM} [27, 59], dynamical screening ν^{LB} [27]

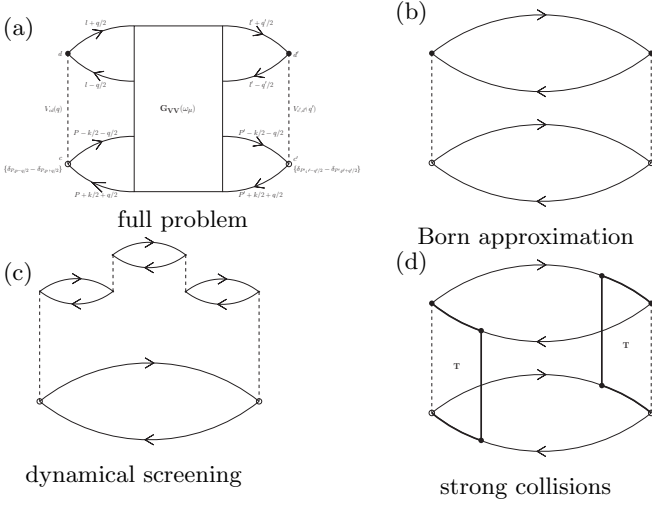


FIG. 4. Feynman-diagrams of electron-particle collisions for a) the ideal solution, b) one realization of weak collisions, c) dynamical screening, and d) strong collisions.

$$\nu^{\text{LB}}(\omega) = i \frac{\varepsilon_0 n_i \Omega_0^2}{6\pi^2 e^2 n_e m_e} \times \int_0^\infty dk k^6 V_{ei}^2(k) S_{ii}(k) \frac{1}{\omega} \left[\frac{1}{\varepsilon_l^{\text{RPA}}(k, \omega)} - \frac{1}{\varepsilon_l^{\text{RPA}}(k, 0)} \right] \quad (7)$$

and weak collisions ν^{Born} , cf. Eq. (5). In the picture of Feynman diagrams, the dynamical screening is calculated by the summation over the ring diagrams, cf. Fig. 4 (c), and strong collisions by performing the partial summation over the ladder diagrams, cf. Fig. 4 (d). To avoid double counting the Born collision frequency is subtracted in Eq. (6) since it is contained in the strong collision and dynamical screening contribution. All used collisional effects used in Eq. (6) are calculated in the low-density and long wavelength limit, $k \rightarrow 0$, where the self-energy correction and three vertex terms are neglected.

Following the predictions of the SCFLY simulations in Fig. 2, our calculations are performed for isochorically heated aluminum with ion densities of $n_i = 6 \times 10^{22} \text{ cm}^{-3}$ and ionization degrees of $Z_{\text{free}} = 3$ leading to electron densities of $n_e = 1.8 \times 10^{23} \text{ cm}^{-3}$. For the electron temperature we use 6 eV (0.2 eV) for the focal spot sizes 1 μm (10 μm), which is determined by comparing measured and calculated scattering spectra. The electron temperature is discussed in subsection IV E.

Fig. 5 shows the real and imaginary part of the calculated dynamical collision frequency for a electron temperature of 6 eV. Due to the degeneracy parameter $\theta_p \approx 0.52 < 1$ and the coupling parameter $\Gamma \approx 2.2 > 1$, a degenerated and strongly coupled plasma is considered. For the calculation of the collision frequency we use the Debye potential

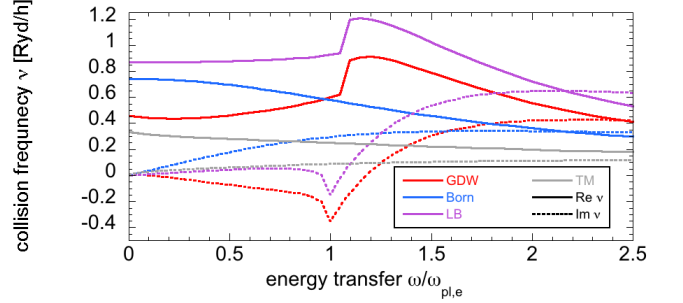


FIG. 5. Real and imaginary part of the calculated collision frequency for electron densities of $n_e = 1.8 \times 10^{23} \text{ cm}^{-3}$ and electron temperatures of $T_e = 6 \text{ eV}$. The calculations use the Debye potential and neglect ionic structure correlations $S_{ii} = 1$.

$$V_{ei}^{\text{D}}(k) = -\frac{e_i e_e}{\varepsilon_0 \Omega_0} \frac{1}{k^2 + \kappa_D^2} \quad (8)$$

with the inverse Debye length

$$\kappa_D^2 = \frac{e^2 m^{3/2}}{\sqrt{2} \pi^2 \varepsilon_0 \hbar^3} \int_0^\infty dE_p E_p^{-1/2} f_p, \quad (9)$$

the Fermi distribution f_p and the particle energy E_p . In addition, we neglect ionic structure correlations $S_{ii}(k) = 1$.

For the real part of the calculated collision frequency in Fig. 5, we observe for $\omega \rightarrow 0$ an almost constant collision frequency that decreases in the high frequency limit to zero. The GDW collision frequency (see Eq. (6)) shows a dominant peak, that is caused by the dynamical screening contribution (see Eq. (7)) and accounts for collective

effects. This can not be observed in the Born collision frequency. For the imaginary part of the GDW collision frequency, we observe negative values. This is not observed in the Born approximation (see Eq. (5)) and stems from the contribution of the dynamical screening (see Eq. (7)).

D. Calculated scattering spectra

The dynamical collision frequencies calculated in the previous subsection, are used to derive the scattering spectrum via the Mermin approximation (MA) of Eq. (4) below. Such collision frequencies were already applied in other works [36, 39, 44, 60] and will be applied here on strongly coupled plasmas.

Fig. 6 shows the measured, calculated and deconvolved x-ray scattering spectra and the source function for a scattering angle of $\theta = 24^\circ$ and focal spot sizes of $1 \mu\text{m}$. The calculations apply the dielectric function in RPA and MA of Eq. (4) considering electron-ion collisions within the Born (see Eq. (5)) and GDW approximation (see Eq. (6)) at electron temperatures of $T_e = 6 \text{ eV}$, cf. Fig. 5. The ion-feature is fitted to the experimental data. The bound-free transitions are not relevant for the considered photon energy shifts below $\approx 50 \text{ eV}$ and are neglected in our calculations. To compare with the measured spectra, the calculated spectra are convolved with the measured source function. The spectrum using MA (best fit) apply collision frequencies extracted from the data and will be discussed in a later subsection.

The convolution of our calculations with the source function show the dominant elastic scattering on bound electrons and the downshifted inelastic scattering on free electrons as observed in the data. However, our calculations can not reproduce the shape of the measured inelastic scattering spectrum. Comparing our calculations with the deconvolved scattering spectra, our results using GDW collision frequencies (see Eq. (6)) can explain the plasmon resonance frequency and the downshifted plasmon slope for energies of $7.96 \text{ keV} < E < 7.98 \text{ keV}$ but not the plasmon width. In contrast to the GDW approximation, neglecting collisions all together (RPA) or using Born collision frequencies (see Eq. (5)), neither of these features can be described.

Our calculated complex dynamical collision frequency often used for weakly coupled plasmas shows in the application on strongly coupled plasma no agreement with the experiment. In contrast to this and former calculations, an advanced potential as well as ionic structure correlations has to be applied. In Sec. V below, we will account for coupling effects considering a pseudopotential and ionic structure correlations in the plasma.

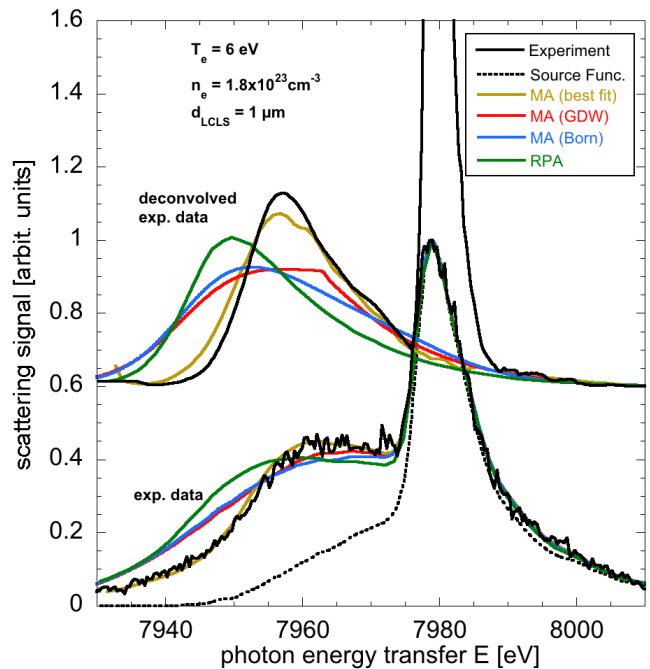


FIG. 6. Measured, calculated and deconvolved spectra and source function as a function of the photon energy for a scattering angle of 24° . The calculations apply RPA (green) neglecting collisions and MA using experimentally extracted (best fit, gold), Born (blue), and GDW (red) collision frequencies. The deconvolved data and calculations are offset by 0.6 for clarity.

E. Determination of the temperature

The extraction of the electrical conductivity from the measured scattering spectra is strongly dependent on an accurate diagnostic of the temperature. The electron temperature can be determined from the comparison of calculated and measured scattering spectrum or from the detailed balance relation [36]

$$\frac{S_{ee}^0(k, \omega)}{S_{ee}^0(-k, -\omega)} = \exp\left(-\frac{\hbar\omega}{k_B T_e}\right). \quad (10)$$

Fig. 7 compares the measured and calculated blue wing of the scattering spectra and the source function for focal spot sizes of 1 and $10 \mu\text{m}$. For the calculations at different electron temperatures, the Mermin approximation of Eq. (4) applying GDW collision frequencies, cf. Eq. (6), is used. The source function defines the scattering signal from the bound electrons shifted to the blue wing due to the non-monochromatic LCLS beam. Therefore, a difference between source function and scattering signal is caused by additional inelastic scattering that can only stem from plasmons. Comparing the blue wing of the experimental spectra and the source functions, we observe an agreement for the data using $10 \mu\text{m}$ focal spot sizes and a disagreements for data using $1 \mu\text{m}$ focal spot sizes.

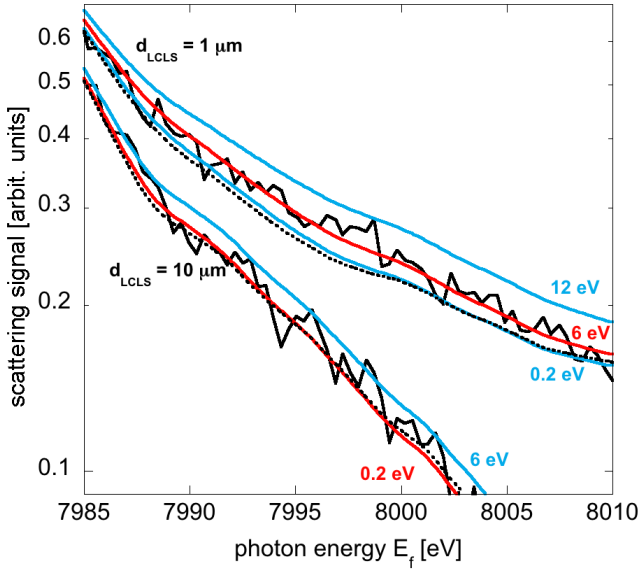


FIG. 7. Blue wing of the measured and calculated x-ray scattering spectra and instrument functions for a focal spot size of 1 and 10 μm (offset by 0.1 for clarity) and scattering angle of 24° . The calculations apply GDW collision frequencies and indicate measured electron temperatures of 6 eV (0.2 eV) for focal spot sizes of 1 μm (10 μm).

This disagreement indicates additional inelastic scattering signal at the blue wing. From that peak, the electron temperature can be determined via the comparison to the calculations shown in Fig. 7 or via comparing with the downshifted plasmon peak within the detailed balance relation Eq. (10).

Here, the electron temperatures were determined by the comparison of the calculated and measured blue wing of the scattering spectrum, where we have applied a least square method. We have allowed a maximal deviation between calculated and measured blue wing of the scattering spectrum of 5%, that leads to an electron temperature of 6(0.2) eV for the focal spot size of 1(10) μm . For the data measured at focal spot sizes of 10 μm only a maximal T_e could be indicated because of the lack of an upshifted plasmon, cf. Fig. 7. The lowest electron temperature which show in the calculations no upshifted plasmon could be found at $T_e = 0.6$ eV.

In Fig. 8 we studied the dependence of the used collision frequency model on the determination of the electron temperature. The calculations use the RPA and the Mermin approximation Eq. (4) applying the Born Eq. (5) and GDW Eq. (6) collision frequency at electron temperatures of $T_e = 6$ eV. Our calculations applying different models show an agreement with the data. In addition, the deviation between the different calculations is less than 5%. Therefore we find only a negligible collision frequency model dependency of the temperature that leads to temperature deviations below 1%.

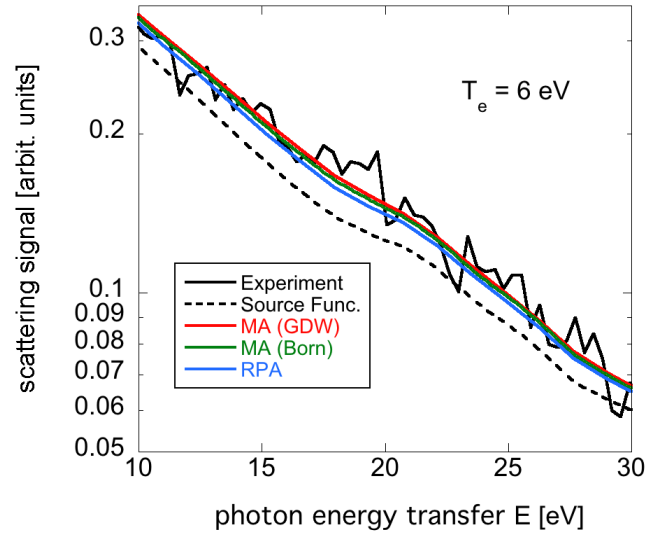


FIG. 8. Blue wing of the measured and calculated x-ray scattering spectrum and the source function for a focal spot size of 1 μm and scattering angle of 24° . The calculations use RPA and MA applying GDW and Born collision frequencies. The blue wing shows only a slight dependency on the used collision frequency.

F. Temporally evolved temperature

Since the scattering spectra is measured during the isochoric heating process of the aluminum target by the LCLS, the scattering spectra characterize a composition of matter states defined by different electron temperatures, cf. Fig. 2. In contrast, our calculations are performed for a single representative temperature. In order to test the influence of the temporally evolving temperature on the scattering spectra, we calculate the scattering spectra as a composition of SCFLY temperatures, see Fig. 2. For that, the calculated spectrum at each time is weighted by the time interval and the FEL intensity. The composition of the spectra for all times results into the characteristic scattering spectrum.

Fig. 9 shows the measured and calculated scattering spectrum and the source function. The MA calculations applying Born collision frequencies (see Eq. (5)) use a single temperature and the temporally evolved SCFLY electron temperature, cf. Fig. 2, respectively. Similar to the findings in Fig. 6, both calculations cannot reproduce the plasmon width as well as the plasmon peak position. In addition, both calculations show an upshifted plasmon resonance peak due to the disagreement to the source function on the blue wing. This peak of the characteristic scattering spectrum defines a characteristic electron temperature of ≈ 5 eV.

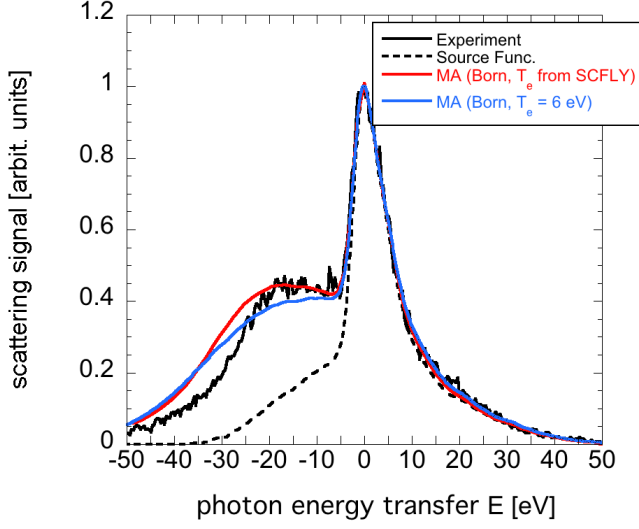


FIG. 9. Measured and calculated scattering spectrum and source function for a focal spot size of $1 \mu\text{m}$ and a scattering angle of 24° . In the calculations, a single representative (blue) as well as a temporal evolved electron temperature (red) is used.

G. Dynamical collision frequencies extracted from the data

For conditions, where the Landau damping is small in comparison to collisions, the free electron contribution of the scattering spectrum is characterized by electron-particle collisions influencing plasmon lifetime and width. In our calculated spectra, the electron-particle collisions are included via the Mermin formula Eq. (4). However, our collisional model cannot explain the data as seen in Fig. 6 by using a Debye potential and neglecting ionic structure correlations. Therefore, we will extract relaxation (collision) frequencies from the data, that is presented below. The relaxation frequencies has to be extracted from the deconvolved spectra. This deconvolution was realized numerically, whose error can not be estimated.

The imaginary part of the inverse longitudinal dielectric function ε_l^{-1} can be extracted from the electronic part of the deconvolved measured scattering power, see Eq. (1), if the fluctuation-dissipation theorem Eq. (3) is applied

$$I_s^{\text{exp}} \sim \frac{\text{Im} \varepsilon_l^{-1}(k, \omega)}{1 - \exp\left(\frac{-\hbar\omega}{k_B T_e}\right)}.$$

This relation needs an exact knowledge of the electron temperature determined before from the data. The normalization of the imaginary part of the inverse longitudinal dielectric function can be realized via the f-sum rule

$$\int_{-\infty}^{\infty} d\omega \omega \text{Im} \varepsilon_l^{-1}(k, \omega, \nu(\omega)) = -\pi \omega_{e,\text{pl}}^2.$$

The plasma frequency $\omega_{e,\text{pl}} = (n_e e^2 / \varepsilon_0 m_e)^{1/2}$ is known from the electron density n_e . The real part of the inverse longitudinal dielectric function can be calculated via the Kramers-Kronig relation

$$\text{Re} \varepsilon^{-1}(k, \omega, \nu(\omega)) = 1 + 2\mathcal{P} \int_0^{\infty} \frac{d\omega'}{\pi} \frac{\omega' \text{Im} \varepsilon^{-1}(k, \omega' + i0, \nu(\omega'))}{\omega'^2 - \omega^2} \quad (11)$$

describing the causality in the system. Due to the contamination of the deconvolved inelastic scattering spectra of the free electrons with the elastic scattering on bound electrons, cf. Fig. 3, the signal for photon frequency shifts below 7 eV has to be neglected. The neglected data was extrapolated to apply the Kramers-Kronig relation Eq. (11) and can influence the results for higher frequency transfers. For that, we have applied the Kramers-Kronig relation on our extracted collision frequency and compare with corresponding extracted real and imaginary part of the frequency, respectively. We find a good agreement for energy transfers above 15 eV and therefore the error of our extracted collision frequencies increases below this energy transfer, see Fig. 10.

With the knowledge of the experimental dielectric function $\varepsilon_l^{\text{exp}}$ from Eq. (11) we can determine the relaxation (collision) frequency ν^{exp} by the numerical comparison with the Mermin dielectric function Eq. (4)

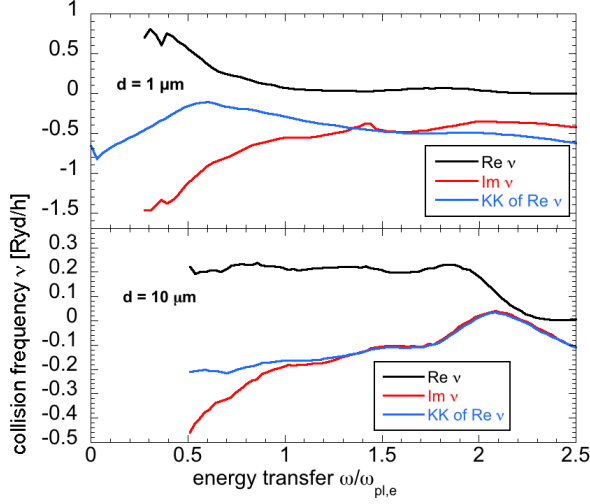


FIG. 10. Real and imaginary part of the collision frequency extracted from the data as a function of the energy per plasma frequency $\hbar\omega_{\text{pl},e} = 15.75$ eV ($n_e = 1.8 \times 10^{23}$ cm $^{-3}$) for a scattering angle of 24° . The results are extracted from the data using 1 (upper panel) and 10 μm (lower panel) focal spot sizes. The Kramers-Kronig relation of the collision frequency indicated in blue are offset by 0.66(0.22) Ryd for focal spot sizes of 1(10) μm .

$$\varepsilon_l^{\text{exp}}(k, \omega, \nu^{\text{exp}}(\omega)) = \varepsilon_l^{\text{M}}(k, \omega, \nu^{\text{exp}}(\omega)).$$

This comparison requires the exact knowledge of electron density and temperature, which are included in ε_l^{M} .

Fig. 10 shows the extracted complex dynamical collision frequency, cf. Fig. 3. For energies below 0.5 $\omega_{\text{pl},e}$ the results are not shown due to the contamination of the inelastic scattering spectra of the free electrons by the elastic scattering on bound electrons. Note, that the imaginary part of the collision frequency has to be zero for $\omega \rightarrow 0$ per definition. In order to compare with the measured data, the extracted collision frequency is applied in the MA (see Eq. (4)). The resulting scattering spectra (MA (best fit)) is shown in Fig. 6 and agrees with the data.

As observed for the calculations in Fig. 5, the real part of the extracted collision frequency in Fig. 10 show for $\omega \rightarrow 0$ an almost constant collision frequency that decreases at a certain energy. This energy is in disagreement with the energy found from the calculated collision frequencies. In disagreement to the GDW approximation, no pronounced peak can be observed.

In agreement to the GDW approximation, the imaginary part of the extracted collision frequency shows negative values. This can not be observed in the Born approximation (see Eq. (5)). Following the GDW approximations, these negative collision frequencies stem from dynamical screening. Furthermore, we observe only a qualitative agreement of the real and imaginary part of

the extracted and calculated collision frequency, whereas a quantitative description of the measurements can not be given. On the one hand, this can be caused by neglecting the ionic correlations and the use of the Debye potential in the calculations. On the other hand, inaccuracies are generated in the deconvolution of the data, the contamination of the inelastic scattering spectrum of the free electrons by the elastic scattering on bound electrons in the extraction, and the subsequent extrapolation of this data for the application of the Kramers-Kronig relation Eq. (11).

V. ELECTRICAL CONDUCTIVITY

A. Dynamical electrical conductivity

With the extraction of the collision frequency from the data, we are able to determine the electrical conductivity in isochorically heated aluminum. In plasmas and metals, the electrical conductivity can be derived from the dynamical electron-particle collisions via the generalized Drude formula [27]

$$\sigma(\omega) = \frac{\varepsilon_0 \omega_{\text{pl},e}^2}{\nu(\omega) - i\omega}. \quad (12)$$

The electrical conductivity characterizes the electrical current induced by an electrical field $\mathbf{J}(\omega) = \sigma(\omega)\mathbf{E}(\omega)$ and is complex in general. The real part of the conductivity defines the field induced current strength whereas the imaginary part determines the phase shift between electrical field and current.

Fig. 11 shows the extracted and calculated real and imaginary part of the electrical conductivity for solid density aluminum at temperatures of $T_e = 6$ eV. The extracted conductivity apply the data measured at angles of $\theta = 24^\circ$ and focal spot sizes of 1 μm , cf. Fig. 10. The calculations apply collision frequencies in Born Eq. (5) and GDW Eq. (6) approximation (see Fig. 5) in the generalized Drude formula Eq. (12). The approximations use a screened Coulomb potential and neglect ionic structure correlations $S_{ii}(k) = 1$. The functional behavior is given by the generalized Drude formula Eq. (12). In order to indicate the experimental error, we show selected points of the extracted electrical conductivity.

Our results show a decreasing real part of the electrical conductivity for increasing frequency transfers in the entire frequency transfer range. The imaginary part goes to zero in the long-wavelength limit ($\omega \rightarrow 0$), shows a maximum and decreases in the high-frequency limit ($\omega \rightarrow \infty$). In comparison to the electrical conductivity defined by Born collision frequencies, the conductivity defined by GDW collision frequencies shows a drop of the real and imaginary part close to the plasma frequency caused by collective effects induced by dynamical screening described by Eq. (7), cf. Fig. 10. In addition, the maximum of the imaginary part is shifted to smaller

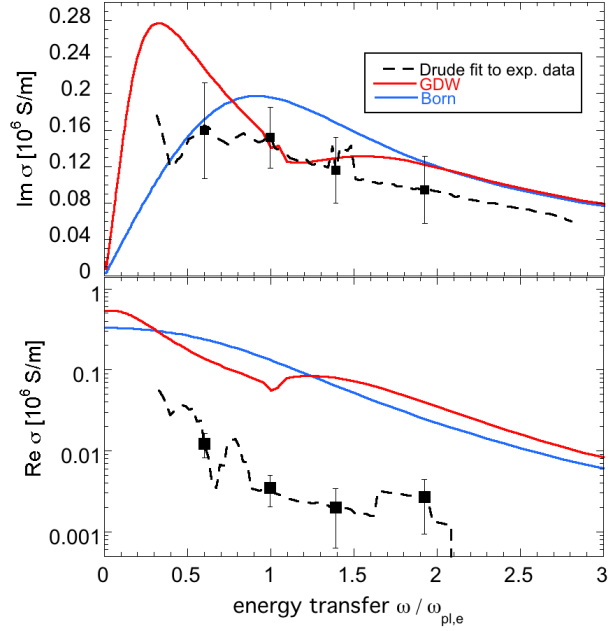


FIG. 11. Real (lower panel) and imaginary (upper panel) part of the electrical conductivity as a function of the frequency transfer per plasma frequency $\hbar\omega_{\text{pl},e} = 15.75$ eV. The electrical conductivity is calculated via the generalized Drude formula Eq. (12) using the extracted, Born, and GDW collision frequencies. The extracted conductivity stems from spectra measured at scattering angles of 24° and focal spot sizes of $1 \mu\text{m}$, cf. Fig. 10, and the Born and GDW collision frequencies are calculated for temperatures $T_e = 6$ eV, cf. Fig. 5. The selected black points are for estimation of the experimental error.

frequency transfers due to the negative imaginary part of the GDW collision frequency. In comparison to these calculations, the imaginary part of the extracted electrical conductivity agrees within the error bars above $0.5 \omega_{\text{pl},e}$ with the generalized Drude calculations using the GDW collision frequencies.

In the long-wavelength limit ($\omega \rightarrow 0$), the real part of the extracted electrical conductivity is comparable to the calculations but for increasing frequency transfers an unpredicted strong decrease is observed which is induced by the negative imaginary part and the fast raise of the real part of the extracted collision frequency, cf. Fig. 10.

B. dc conductivity

As long-wavelength limit ($\omega \rightarrow 0$), the dc conductivity can be calculated from the generalized Drude expression of Eq. (12) via $\sigma_{\text{dc}} = \varepsilon_0 \omega_{\text{e,pl}}^2 / \nu(0)$. The static collision frequency $\nu(0)$ can be calculated from the Born and GDW approximation, cf. Fig. 5. However, the dc conductivity cannot be inferred directly from the extracted electrical data shown in Fig. 11 due to the contamina-

tion of the scattering signal from the free electrons by bound electron scattering contributions. Instead, we follow the theoretical predictions, that the real part of the collision frequency can be assumed as almost constant for $\omega < 0.5 \omega_{\text{pl},e}$, cf. Fig. 5. Therefore, we apply for the dc conductivity the extracted electrical conductivity for $\omega \rightarrow 0$, cf. Fig. 11. For $\omega = 0$, the imaginary part of the collision frequency has to be zero by definition.

Fig. 12 shows the dc conductivity extracted from the data of this work, of the experiments of Milchberg et al. [16], Gathers [61], Desai et al. [62] and of theoretical models of Spitzer and Härm [26], Faussurier and Blancard [63], Lee and More [25], and the Drude approach using collision frequencies in Born and GDW approximation. In the Spitzer and Lee and More model, the approximation of the effective quantum Coulomb logarithm in Ref. [65] was applied. This Coulomb logarithm was calculated within a Born approximation using the Debye potential. The model of Faussurier and Blancard applies a average-atom model [66].

For our collision frequency calculated via the Born approximation Eq. (5), we use a screened Coulomb potential and neglect ionic structure correlations $S_{\text{ii}}(k) = 1$. The resulting dc conductivity is indicated as (Born Coulombpot.) in Fig. 12. In order to account also for ionic structure correlations and degeneracy effects in strongly coupled plasmas, we apply a pseudopotential accounting for degeneracy effects, e.g., Pauli-blocking, and an ionic structure factor $S_{\text{ii}}(k)$, accounting for ionic structure correlations. This model is explained in the next subsection. In Fig. 12 this calculation is indicated as (Born pseudopot.).

Our calculations and measurements show for temperatures below the Fermi energy $E_F \approx 12$ eV, that the dc conductivity increases for decreasing temperatures caused by ionic structure correlations and electron-ion repulsions not explainable by the model of Spitzer. For temperatures above the Fermi energy a rising dc conductivity is observed, that is induced by excited electrons in the conduction band. Here it is to mention, that our calculations assume for all temperatures a mean ionization degree of $Z_f = 3$.

Within our experiments, we find at temperatures of $T_e = (0.2 \pm 0.1)$ eV a dc conductivity of $\sigma_{\text{dc}} = (1.3 \pm 0.7) \times 10^6$ S/m. This finding is slightly below the measured dc conductivities of Gathers 2.3×10^6 S/m, but agrees within the temperature and conductivity error bars. Here it is to mention, that the experimental electron temperature could only determined in a range below 0.6 eV due to the lack of an upshifted plasmon.

At temperatures of $T_e = (6 \pm 0.5)$ eV our result $(0.36 \pm 0.12) \times 10^6$ S/m agrees within the error bars with our model using Born collision frequencies applying a Coulombpotential 0.37×10^6 S/m and a pseudopotential 0.46×10^6 S/m. Here, our measurement is smaller than our calculations using GDW collision frequencies [27], 0.59×10^6 S/m, and larger than the models of Lee and More [25], 0.24×10^6 S/m.

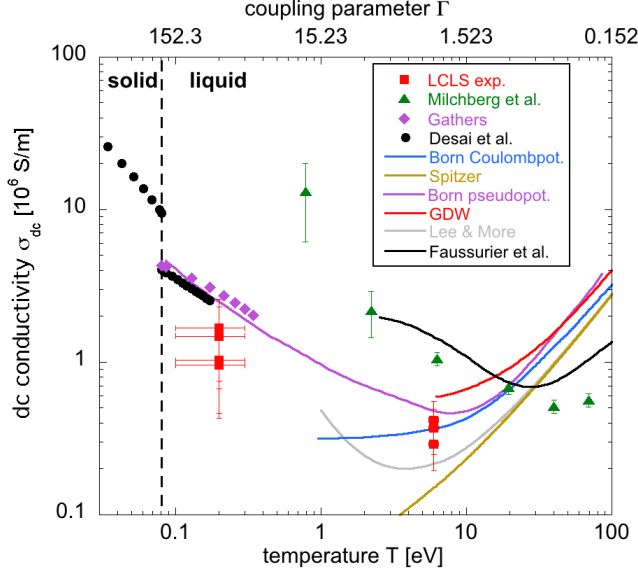


FIG. 12. dc conductivity as a function of temperature for solid density aluminum $\rho = 2.7 \text{ g/cm}^3$ and a mean ionization degree of $Z_f = 3$ (figure from [35]). Extracted results, experimental results of Desai et al., Gathers, and Milchberg et al. and theoretical models of Lee and More, Spitzer, Faussurier et al., and the generalized Drude model using GDW and Born collision frequencies. The Born collision frequency applies a screened Coulomb potential (Coulombpot., blue line) and ionic structure correlations and a pseudopotential including temperature-dependent Pauli blocking (pseudopot., violet line).

In contrast to former conductivity measurements of Milchberg et al. [16] at $T_e = 6 \text{ eV}$, $1.053 \times 10^6 \text{ S/m}$, our results show smaller dc conductivities. They have measured the conductivity via optical laser reflectivity that results into ac conductivities. Following works [22, 67] have suggested corrections by downshifted temperatures after comparing with theoretical estimations. These suggestions are motivated by the inaccurate temperature determination within the experiment of Milchberg et al. [16], where the temperature was determined separately by radiation-hydrodynamic simulations. In contrast, we could determine the electrical conductivity and temperature from the experiment.

C. Calculation of the dc conductivity considering warm dense matter effects

The collision frequency in Born approximation applying a screened Coulomb potential and neglecting ionic structure correlations $S_{ii}(k) = 1$ [39, 44] often used in plasma physics could not reproduce the extracted dc conductivity (see Fig. 12) in the strongly coupled liquid aluminum phase close to the melting point. Instead, we include for the considered conditions more realistic ionic structure correlations and electron-ion potentials. As

shown in Fig. 12, such an approach can reproduce our measurements, see Ref. [68, 69]. In this subsection we will present this approach, which has to be valid for the temperature interval $0.08 \text{ eV} < T < 100 \text{ eV}$. Therefore, we require within this interval a temperature dependence of the ionic structure factor $S_{ii}(k)$ and the electron-ion potential $V_{ei}(k)$.

The collision frequency in Born approximation Eq. (5) simplifies in the long-wavelength limit [70, 71], so that the dc conductivity can be expressed by [72]

$$\begin{aligned} \sigma_{\text{dc}}^{\text{Born}} &= \frac{\varepsilon_0 \omega_{\text{pl},e}^2}{\nu^{\text{Born}}(0)} \\ &= \frac{12\pi^3 e^2 \hbar^3 n_e}{m^2 \Omega_0^2} \left[\int_0^\infty dk k^3 V^2(k) S_{ii}(k) f_{k/2} \right]^{-1}. \end{aligned} \quad (13)$$

This approximation takes into account the ionic structure correlations via the ionic structure factor $S_{ii}(k)$ and the electron-ion pseudopotential $V_{ei}(k)$. In what follows, we will take into account expressions for $S_{ii}(k)$ and $V_{ei}(k)$ which are suited to model the strongly coupled plasma regime of aluminum in dependence on the temperature.

1. Ionic structure correlations

The ionic structure correlations in Eq. (13) has to be known in a wide temperature interval. On the one hand, measurements of $S_{ii}(k)$ in liquid aluminum up to $T = 0.1$ eV exist [73, 74], which are well-described by hard-sphere models of the Percus-Yevick (PY) expression [68, 75]

$$S_{ii}(\zeta) = \frac{1}{1 - C(\zeta)}, \quad (14)$$

with

$$C(\zeta) = -24\eta \int_0^1 ds \quad (15)$$

$$s^2 \frac{\sin(s\zeta)}{s\zeta} \left[\frac{(1+2\eta)^2}{(1-\eta)^4} - 6\eta \frac{(1+\eta/2)^2}{(1-\eta)^4} s + \frac{\eta(1+2\eta)^2}{2(1-\eta)^4} s^3 \right],$$

the parameter $\zeta = 2kr_{hc}$, the filling factor $\eta = 8(\pi/6)n_i r_{hc}^3$, and the ion density n_i . By comparing with measurements of the ionic structure factor in liquid solid density aluminum $\rho = 2.7$ g/cm³ with the melting temperature of $T_m = 0.08$ eV [73, 74], the hard-core radius $r_{hc} = 2.39$ a_B and the filling factor $\eta \approx 0.45$ could be determined. In addition, the change of η with T near the melting point has been extracted from the measured structure factor.

On the other hand, in the high-temperature limit of aluminum plasmas the ionic structure factor is given by the Debye expression

$$S_{ii}(k) = \frac{k^2 + \kappa_e^2}{k^2 + \kappa_e^2 + \kappa_i^2} \quad (16)$$

with the inverse screening lengths κ_e, κ_i , cf. Eq. (9). For the WDM we have to interpolate between the liquid and plasma case. In order to describe the ion structure factor for temperature between these limits, we use Classical-Map HyperNetted-Chain (CHNC) calculations [76]. In the high temperature limit, the CHNC calculations coincide with the Debye approximation, whereas results for temperatures $T < 1$ eV, in particular liquid aluminum, are not reliable, see Appendix. A 1.

Fig. 13 shows the measured [73] and calculated ion structure factor $S_{ii}(k)$ for aluminum at solid density and different temperatures. The calculations apply the PY expression, CHNC calculations and the Debye model. In the liquid aluminum phase, for temperatures close to the melting point $T_m \approx 0.08$ eV, we find a good agreement between measurement and the PY expression Eq. (14). Of particular interest for the determination of the conductivity is the first peak of $S_{ii}(k)$, and we consider the position of the maximum of this peak as characteristic. For higher temperatures the PY is not valid and shows no agreement with CHNC and, as limiting case, with the Debye results. For $T = 8.6$ eV we find an almost

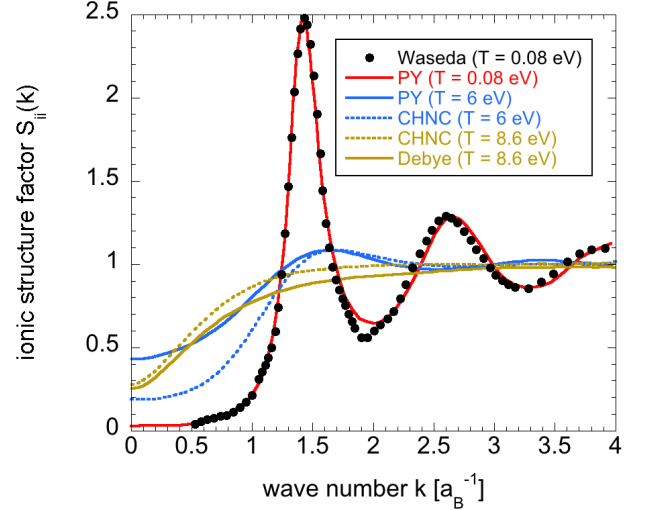


FIG. 13. Measured [73] and calculated dynamic ion structure factor $S_{ii}(k)$ of solid density aluminum $\rho = 2.7$ g/cm³ as a function of the wave number for different temperatures. The calculations use the PY expression (see Eq. (14)), CHNC [76], and the Debye approximation (see Eq. (16)).

uncorrelated system. Here, S_{ii} can be approximated by the Debye expression Eq. (16). For temperatures below $T < 1$ eV the CHNC calculations yield a correct position of the first correlation peak in the ionic structure factor, but overestimates the first peak maximums S_{ii}^{\max} in comparison with the experimental data around the melting point [73, 77]. Therefore, we combine PY and CHNC in a simple way by determining the PY parameters r_{hc}, η at $T = 6$ eV by the first peak position and maximum calculated by CHNC. Despite discrepancies of CHNC and PY at $T = 6$ eV at low wave number k , the resulting conductivity changes are below 1% because of the suppression of the low- k contributions in Eq. (13). From this temperature down to the melting point an interpolation of the PY parameters as function of T has been performed. This combination of CHNC and PY calculations is shown in Appendix A 1.

2. Pseudopotential

The theory of dc conductivity in liquid metals has been worked out on the basis of the Ziman formula (13), and excellent results have been obtained using appropriate expressions for the electron-ion pseudopotential, see Ref. [78]. In particular, the dc conductivity of aluminum near the melting point was well reproduced [68, 69]. Our approach to WDM should implement the properties near the melting point as a benchmark.

In order to model the electron-ion potential V_{ei} in a strongly coupled and degenerated system, we apply in the Born approximation Eq. (13) the potential of Schneider and Stoll [69]

$$\begin{aligned}
V_{ei}(k) &= \frac{V_{ei}^{\text{ps}}(k)}{1 + W(k)} \\
V_{ei}^{\text{ps}}(k) &= (n_i \Omega_0)^{-1} \left[-\frac{Z n_i e^2}{\epsilon_0 k^2} + \gamma_1 H_1(kr_1) + \gamma_2 H_2(kr_2) \right], \\
W(k) &= \frac{\kappa_{\text{TF}}^2}{k^2} \left(1 - \frac{1}{2} \frac{k^2}{k^2 + 2.39 k_F^2} \right) f(k/(2k_F)), \\
f(t) &= \frac{1}{2} + \frac{1-t^2}{4t} \ln \left| \frac{1+t}{1-t} \right|.
\end{aligned} \tag{17}$$

Here, $k_F = \sqrt[3]{3\pi^2 n_e}$ is the Fermi wave number, $\kappa_{\text{TF}}^2 = e^2 m (3Z n_i / \pi)^{1/3} / (\pi \epsilon_0 \hbar^2)$ is the Thomas-Fermi screening parameter, and Ω_0 is the normalization volume. For the pseudopotential V_{ei}^{ps} a composition of the long-range Coulomb potential and Pauli repulsion, represented by the overlap of hydrogenic core wave functions (s and p -like orbitals) and a plane wave function

$$H_1 = \frac{1}{(1 + (kr_1)^2)^2}, \quad H_2 = \frac{kr_2}{(1 + (kr_2)^2)^3},$$

was applied. The parameters γ_n and r_n at the melting point of aluminum are obtained from comparisons with measured phonon dispersion relations [69] ($r_1 = 0.32$ aB, $r_2 = 0.30$ aB, $\gamma_1 = 0.338$ Ryd and $\gamma_2 = 0.163$ Ryd). Using this pseudopotential together with appropriate expressions for the structure factor Schneider and Stoll [69] could reproduce the electrical conductivity measured in liquid solid density aluminum $\rho = 2.7$ g/cm³ close to the melting point. A similar method was also used by Ashcroft and Lekner [68].

Within the WDM approach, we have to go from the temperatures near the melting point to high temperatures where a plasma description is applicable. This refers also to the electron-ion pseudopotential which has to be considered as a temperature-dependent quantity. Considering the expression (17), the screening expression by the contribution $W(k)$ has to be replaced by a temperature dependent term known from the RPA expression for the dielectric function, which interpolates between the Thomas-Fermi and the Debye limit, so we replace κ_{TF}^2 with κ_D^2 , see Eq. (9). In addition, the Pauli repulsion term in Eq. (17) have to be considered as function of T . Originated by the antisymmetrization of the wave function, this exchange interaction is non-local and can only approximately represented by a local, energy-dependent potential. In extension to Ref. [69], we consider the parameters γ_1, γ_2 as function of T to use the pseudopotential within a wide temperature range. In particular, we use temperature dependent parameters $\gamma_1 = 0.336 e^{-2T/13.6 \text{ eV}}$ Ryd and $\gamma_2 = 0.162 e^{-2T/13.6 \text{ eV}}$ Ryd, as motivated in Appendix B. The temperature effects are caused by screening which interpolates between Thomas-Fermi screening in the degenerated case and Debye screening in the non-degenerated case. In addition, we have included the Pauli

blocking in the s and p orbitals characterized by the parameter $\gamma_1 H_1^2$ and $\gamma_2 H_2^2$, respectively.

If we compare in Fig. 12 the Born approximation using a pseudopotential and ionic structure correlations with the approximation using the Debye potential and neglecting ionic structure correlations, we find a large discrepancy for temperatures below 6 eV. Applying such pseudopotentials and ionic structure correlations, we observe an agreement of our measured and calculated dc conductivity for temperatures of $T = 6$ eV as well as close to the melting point.

3. Dynamical electrical conductivity

After the influence of the ionic structure factor and the electron-ion pseudopotential on the dc conductivity has been discussed, it is evident that also the dynamic (ac) conductivity is changed in an essential way if these quantities are taken into account. According to Eq. (13), also the dynamical collision frequency is modified if the ionic structure factor and the electron-ion pseudo potential is taken into account, as already seen in the Born approximation, Eq. (5). Whereas in Sec. IV C the correlations between the ions has been neglected, $S_{ii}(k) = 1$, and the screened Coulomb potential has been considered instead of the pseudopotential $V_{ei}^{\text{ps}}(k)$, we discuss now the change of the dynamical collision frequency if these effects are taken into account.

We stay in the Born approximation, higher order terms such as T matrix and dynamical screening have also an essential influence on the dynamical collision frequency $\nu(\omega)$ as discussed in Sec. IV C for the pure Coulomb interaction but will not be considered here.

Let us discuss the real part of the dynamical collision frequency in Born approximation, long-wavelength limit, for a general, non-local form of the electron-ion interaction $V(p, q, \alpha, \alpha')$

$$\begin{aligned}
\text{Re } \nu^{\text{Born}}(\omega) &= -\frac{\pi \beta \hbar}{mN} \frac{e^{-\beta \hbar \omega} - 1}{-\beta \hbar \omega} \sum_{p, k, \alpha, \alpha'} \frac{k^2}{3} \\
&\times |V(p, k, \alpha, \alpha')|^2 S_{ii}(k) \delta(\hbar \omega + E_{p+k} - E_p) f_{p+q} (1 - f_p)
\end{aligned} \tag{18}$$

which is valid for any degeneracy (see Ref. [79]). Here, α describes the internal state of the core electrons of the ion which can be excited to α' by the interaction with an electron, momentum p changing to $p + k$. For more discussions see Appendix B. Neglecting excitations of the internal state α and considering local interactions, i.e. depending only on k , but not on the momentum p , the expression for the dc conductivity given above are recovered in the limit $\omega \rightarrow 0$. The imaginary part of $\nu^{\text{Born}}(\omega)$ follows from the Kramer-Kronig relation.

The account of the ionic structure factor $S_{ii}(k)$ in the dynamical collision frequency Eq. (5) can immediately performed, as already discussed for the case of static collision frequency Eq. (13). Using the interpolation be-

tween the PY expression Eq. (14) and the CHNC results given in the previous section, only small modifications are obtained. In contrast, the pseudopotential will have a strong influence on the dynamical collision frequencies, in particular the behavior at large k values. For instance, we can use the Schneider/Stoll expression for the pseudopotential [69] given above. The treatment of finite frequencies in the pseudopotential for the dynamical case is problematic because of the effective, non-local, dispersive potential. The Pauli blocking terms determined by the orbitals of the core electrons are sensitive to the energy, in contrast to the Coulomb interaction which is local and non-dispersive. This means that the parameters γ_1, γ_2 should be considered not only as a function of the temperature T but also of the frequency transfer ω . If a similar suppression as with T is also assumed with ω , at very high frequencies only the screened Coulomb potential remains leading to higher values for the real part of the Born collision frequency $\text{Re } \nu^{\text{Born}}(\omega)$ Eq. (18). This tendency that $\text{Re } \nu^{\text{Born}}(\omega)$ is not going down at the plasma frequency, is also seen in the data observed for focal spot sizes of $10 \mu\text{m}$ shown in Fig. 10. At high temperatures, the Pauli blocking terms are already suppressed so that the reduction happens earlier.

We will not go here in more details. In order to model the frequency and temperature dependent ionic structure correlations and pseudopotentials DFT-MD calculations can be performed. By this way more reliable results for the dynamical collision frequency $\text{Re } \nu^{\text{B}}(\omega)$ are expected.

VI. CONCLUSIONS AND OUTLOOK

We successfully studied highly resolved plasmons by x-ray Thomson scattering in warm dense aluminum isochorically heated and probed with the seeded LCLS beam. We obtained down- and up-shifted plasmons that provide an accurate measurement of the electron temperature. The highly accurate measurements allowed us to infer the microscopic collisional properties of WDM and determine the macroscopic properties, i.e. the complex dynamical electrical conductivity. Compared to our quantum statistical theory, the imaginary part of the dynamical conductivity agrees but discrepancies for the real part persist.

Using standard relations, we also infer the dc conductivity which could be reproduced in the warm dense matter as well as near the melting point by applying the Born approximation. We take into account ionic structure correlations as well as temperature dependent Pauli-blocking and could reproduce our experimental findings.

In the present work, some semi-empirical concepts such as the pseudopotential and the parametrization of the ionic structure factor have been used which may be improved using more sophisticated approaches, in particular DFT-MD simulations.

The measurement of dc conductivities is important for modeling inertial confinement fusion plasma generation

and the assembly of the fuel capsules. However, accurate measurements of the electrical conductivity for these plasma regimes not exist but are strongly needed. Applying this newly developed technique to pump-probe experiments using optical lasers as pump and hard x-ray FEL as probe will also allow to infer the electrical conductivity of plasma states relevant for modeling the magnetic field generation of planets and stars. Hence our results provide strongly needed accurate measurements of electrical conductivities, which will give important impulses to develop new models for transport properties within dense plasmas.

ACKNOWLEDGEMENTS

We like to thank B. Witte, H. Rüter, R. Redmer and R. Bredow for helpful discussions and providing ionic structure factors from CHNC calculations. This work was performed at the Matter at Extreme Conditions (MEC) instrument of LCLS, supported by the DOE Office of Science, Fusion Energy Science under contract No. SF00515. This work was supported by DOE Office of Science, Fusion Energy Science under FWP 100182 and the DFG within SFB 652. This work was further supported by Laboratory Directed Research and Development grant, the Alexander von Humboldt Foundation, and the Volkswagen Foundation.

Appendix A: Temperature dependent ionic structure correlations and Pauli-blocking

1. Interpolated ionic structure factor

As already explained in Sec. VC 1 the ionic structure factor within a temperature interval of $0.08 \text{ eV} < T < 6 \text{ eV}$ was interpolated between CHNC and PY Eq. 14 calculations. For temperatures below $T < 1 \text{ eV}$ the CHNC calculations yield a correct position of the first correlation peak in the ionic structure factor, but overestimates the first peak maximums S_{ii}^{max} in comparison with the experimental data around the melting point [73]. Therefore, we combine PY and CHNC in a simple way by determining the PY parameters r_{hc}, η by the first peak positions calculated by CHNC at $T = 6 \text{ eV}$. The first peak maximums are used from the PY result. At temperatures close to the melting point we know the PY-parameters by comparison with the experimental data, see Tab. I. On the other hand for high temperatures we determine the PY parameters by comparison with the CHNC calculations, see Tab. I. The PY-parameter η determines the maximum, whereas the parameter r_{hc} determines the position of the first correlation peak. These parameters are interpolated between the temperature $T = 0.08 \text{ eV}$ and $T = 6 \text{ eV}$. Assuming correct peak positions in the CHNC calculations the PY-parameter r_{hc} is adjusted.

The temperature dependent filling parameter η is fitted by $\eta(T) = 0.192/\sqrt[3]{T[\text{eV}]}$, that reproduces within the PY expression the experimental data at the melting point [73, 74]. In contrast to the exponential fit suggested by

Waseda et al. [73] $\eta^W(T) = 0.613 \exp(-3.992 T[\text{eV}])$ which is not applicable in the plasma region, our fit agrees also with the CHNC calculations at $T = 6 \text{ eV}$. For $T > 6 \text{ eV}$, the CHNC results are used.

$T [\text{eV}]$	measured first peak position [73] [a_B^{-1}]	measured first peak maximum S_{ii}^{max}	CHNC first peak position [a_B^{-1}]	CHNC first peak maximum S_{ii}^{max}	PY η	PY $r_{\text{hc}} [a_B]$	PY first peak position [a_B^{-1}]	PY first peak maximum $S_{ii}^{\text{max}}(\eta)$
0.08	1.43	2.475	-	-	0.45	2.39	1.43	2.513
0.09	1.43	2.271	-	-	0.43	2.36	1.43	2.304
0.11	1.43	1.934	-	-	0.40	2.32	1.43	1.975
0.17	-	-	1.43	3.88	0.35	2.26	1.43	1.709
0.43	-	-	1.42	2.41	0.25	2.18	1.43	1.370
0.86	-	-	1.42	1.81	0.20	2.12	1.43	1.246
1.72	-	-	1.45	1.44	0.16	2.07	1.45	1.172
6.03	-	-	1.61	1.10	0.11	1.84	1.61	1.096
8.62	-	-	1.74	1.06	0.09	1.69	1.74	1.083

TABLE I. Measured [73] and calculated position and maximum S_{ii}^{max} of the first correlation peak in the ionic structure factor $S_{ii}(k)$, cf Fig. 13. The calculations apply CHNC and the PY approximation. Shown is also the filling parameter η and the hard sphere radius r_{hc} used in the PY calculations to reproduce the measured and the CHNC results.

Appendix B: Temperature dependent Pauli-blocking

In order to give an argument for the reduction of Pauli blocking at increasing temperature as mentioned in Sec. V C 2, we start from the single-particle in-medium equation

$$(\hat{h} - E_n)|\psi_n\rangle + \hat{B}\hat{V}|\psi_n\rangle = 0, \quad (\text{B1})$$

where the single-particle Hamiltonian \hat{h} contains the quasiparticle mass, \hat{V} the (mean-field) Coulomb interaction with the core ion, and $\hat{B} = 1 - \sum_m^{\text{occ}} |\psi_m\rangle\langle\psi_m|$ contains the Pauli blocking, in particular by the core electrons. At finite temperatures, we describe the occupation of the phase space by the Fermi distribution function, in homogeneous matter $f(\mathbf{p}; \mu, T) = [\exp(\beta E_p - \beta \mu) + 1]^{-1}$ and $\hat{B} = 1 - \sum_p f(\mathbf{p}; \mu, T) |\mathbf{p}\rangle\langle\mathbf{p}|$. \hat{B} is diagonal in momentum space for homogeneous matter, it is depending on the chemical potential μ or, correspondingly, the electron density n according to the well-known equation of state $n = \sum_p f(\mathbf{p}; \mu, T)$ (spin variable is dropped).

To describe the motion in a potential, it is advantageous to pass to the position representation. Using the complete set of single-particle eigenstates $|\psi_m\rangle$, we have

$$\begin{aligned} V(\mathbf{p}; \mathbf{p} + \mathbf{k}) &= \langle \mathbf{p} | \hat{B} \hat{V} | \mathbf{p} + \mathbf{k} \rangle \\ &= \int d^3 r_1 \int d^3 r_2 \sum_m \psi_m(\mathbf{r}_1) \psi_m^*(\mathbf{r}_2) [1 - f(E_m; \mu, T)] \\ &\quad \times \frac{-Ze^2}{4\pi\epsilon_0 |\mathbf{r}_2|} e^{i\mathbf{p} \cdot \mathbf{r}_1 - i(\mathbf{p} + \mathbf{k}) \cdot \mathbf{r}_2} \\ &= \int \frac{d^3 q}{(2\pi)^3} \frac{Ze^2}{\epsilon_0 q^2} \int d^3 r \int d^3 R [\delta^3(\mathbf{r}) - f^{\text{Wigner}}(\mathbf{r}, \mathbf{R}; \mu, T)] \\ &\quad \times e^{i\mathbf{r} \cdot (\mathbf{p} + \mathbf{q}/2 - \mathbf{k}/2) - i\mathbf{R} \cdot (\mathbf{q} - \mathbf{k})}, \end{aligned} \quad (\text{B2})$$

where relative ($\mathbf{r} = \mathbf{r}_2 - \mathbf{r}_1$) and c.o.m. coordinates ($\mathbf{R} = (\mathbf{r}_1 + \mathbf{r}_2)/2$) have been introduced, and $f^{\text{Wigner}}(\mathbf{r}, \mathbf{R}; \mu, T) = \sum_m \psi_m(\mathbf{R} - \mathbf{r}/2) \psi_m^*(\mathbf{R} + \mathbf{r}/2) f(E_m; \mu, T)$ is the Wigner distribution function.

In a homogeneous Fermi gas (no dependence on R), the integral over R yields $\delta^3(\mathbf{q} - \mathbf{k})$. According Eq. (B1) the Coulomb interaction is replaced by

$$V(\mathbf{p}; \mathbf{p} + \mathbf{k}) = \frac{Ze^2}{\epsilon_0 \Omega k^2} \left[1 - \int d^3 r f_{\text{hom}}^{\text{Wigner}}(\mathbf{r}; \mu, T) e^{i\mathbf{p} \cdot \mathbf{r}} \right]. \quad (\text{B3})$$

With plane wave eigenstates $|\psi_m\rangle$ corresponding to the homogeneous Fermi gas, we have at zero temperature $T = 0$ the Wigner distribution function

$$\begin{aligned} f_{\text{hom}}^{\text{Wigner}}(\mathbf{r}; \mu, T = 0) &= \int \frac{d^3 p}{(2\pi)^3} f(\mathbf{p}; \mu, T = 0) e^{i\mathbf{p} \cdot \mathbf{r}} \\ &= \frac{1}{2\pi^2 r^3} [-p_F r \cos(p_F r) + \sin(p_F r)], \end{aligned} \quad (\text{B4})$$

p_F denotes the Fermi momentum. For finite T this result has to be modified. In the classical limit we obtain (Rydberg units)

$$f_{\text{hom}}^{\text{Wigner}}(r; \mu, T) = \int \frac{d^3p}{(2\pi)^3} \frac{n\Lambda^3}{2} e^{-p^2/T} e^{i\mathbf{p}\cdot\mathbf{r}} = \frac{1}{2} n e^{-Tr^2/4}. \quad (\text{B5})$$

The Pauli blocking term is suppressed with increasing temperature according to the exponential term $e^{-Tr^2/4}$. To give an estimation, a characteristic value \hat{r} is of interest. In Eq. (B2) the interference term $e^{i\mathbf{r}\cdot(\mathbf{p}+\mathbf{q}/2-\mathbf{k}/2)}$ is washed out for $pr \approx \pi$. For the scattering processes considered here, the momentum p is near the Fermi momentum p_F , $\hat{p} \approx 1/a_B$ so that $\hat{r} \approx \pi a_B$. This gives an estimation $e^{-(\pi^2/4)T/13.6\text{eV}}$ for the suppression factor of the Pauli repulsion term.

In case of an inhomogeneous Fermi gas, the density $n(\mathbf{R})$ or the chemical potential $\mu(\mathbf{R})$ are depending on the position \mathbf{R} . The local density approximation where the density or the chemical potential are depending on the position \mathbf{R} in a parametric way, can be applied for a smooth dependence on \mathbf{R} so that gradient terms can be neglected. A more detailed analysis of Eq. (B2) using a density distribution $n(\mathbf{R})$ of the core electrons, i.e. $f^{\text{Wigner}}(\mathbf{r}, \mathbf{R}; \mu, T) \approx f_{\text{hom}}^{\text{Wigner}}(\mathbf{r}; \mu(\mathbf{R}), T)$, is not intended in the present section.

Appendix C: Model calculation of the Pauli repulsion interaction

To discuss the effects of the Pauli repulsion interaction as introduced by the pseudopotential, Eq. (17), we consider a simple model where a positive nucleus, charge Ze , is surrounded by bound electrons. The origin of the pseudopotential is the additional exchange interaction with these core electrons which leads, as a consequence of the Pauli blocking, to a repulsion. For simplicity we consider the core electron in the orbit

$$\psi_\alpha(\mathbf{r}) = (\pi a_{\text{eff}}^3)^{-1/2} e^{-r/a_{\text{eff}}} \quad (\text{C1})$$

with the effective radius a_{eff} . The matrix element of the interaction of an electron, momentum \mathbf{p} with the ion, internal state α (we assume the adiabatic limit where the momentum \mathbf{p}_i of the ion is not relevant) and momentum transfer \mathbf{k} is given by

$$\begin{aligned} V(\mathbf{p}, \mathbf{p} + \mathbf{k}, \alpha, \alpha') &= \langle \mathbf{p}, \alpha, \mathbf{p}_i | \mathbf{r}_e, \mathbf{r}_c, \mathbf{r}_i \rangle \\ &\times \left(-\frac{Ze^2}{4\pi\epsilon_0 |\mathbf{r}_e - \mathbf{r}_i|} + \frac{e^2}{4\pi\epsilon_0 |\mathbf{r}_e - \mathbf{r}_c|} \right) \\ &\times \langle \mathbf{r}_e, \mathbf{r}_c, \mathbf{r}_i | \mathbf{p} + \mathbf{k}, \alpha', \mathbf{p}_i - \mathbf{k} \rangle. \quad (\text{C2}) \end{aligned}$$

For equal spin orientation of the core electron at \mathbf{r}_c and the interacting free electron at \mathbf{r}_e , the wave function

$\langle \mathbf{r}_e, \mathbf{r}_c, \mathbf{r}_i | \mathbf{p}, \alpha, \mathbf{p}_i \rangle$ must be antisymmetrized,

$$\begin{aligned} \langle \mathbf{r}_e, \mathbf{r}_c, \mathbf{r}_i | \mathbf{p}, \alpha, \mathbf{p}_i \rangle &= \frac{1}{\Omega} \frac{1}{\sqrt{N_{p,\alpha}}} e^{i\mathbf{p}_i \cdot \mathbf{r}_i} \\ &\times [e^{i\mathbf{p} \cdot \mathbf{r}_e} \psi_\alpha(\mathbf{r}_c - \mathbf{r}_i) - e^{i\mathbf{p} \cdot \mathbf{r}_c} \psi_\alpha(\mathbf{r}_e - \mathbf{r}_i)] \quad (\text{C3}) \end{aligned}$$

with the normalization volume Ω and the normalization factor $N_{p,\alpha} = 2 - (2/\Omega)[8\sqrt{\pi}a_{\text{eff}}^{3/2}/(1 + a_{\text{eff}}^2 p^2)]^2$ for the 1s-like state of the core electron.

The evaluation of the matrix element of the interaction gives eight contributions, we focus here only on the direct term of the $e - i$ interaction $V_d(\mathbf{p}, \mathbf{p} + \mathbf{k}, \alpha, \alpha') = -Ze^2/(\epsilon_0 \Omega k^2) \delta_{\alpha,\alpha'}$ what is the well-known Coulomb interaction, and the exchange term

$$\begin{aligned} V_{\text{ex}}(\mathbf{p}, \mathbf{p} + \mathbf{k}, \alpha, \alpha') &= \frac{Ze^2}{4\pi\epsilon_0 \Omega} \int d^3r_e \psi_\alpha(\mathbf{r}_e) \frac{1}{r_e} e^{-i(\mathbf{p}+\mathbf{k}) \cdot \mathbf{r}_e} \\ &\times \int d^3r_c e^{-i\mathbf{p} \cdot \mathbf{r}_c} \psi_{\alpha'}^*(\mathbf{r}_c) \\ &= \frac{8a_{\text{eff}}^2 Ze^2}{\epsilon_0 \Omega (1 + a_{\text{eff}}^2 p^2)^2 (1 + a_{\text{eff}}^2 (\mathbf{p} + \mathbf{k})^2)} \quad (\text{C4}) \end{aligned}$$

if we consider only the 1s-like internal quantum state α , Eq. (C1), of the core electron.

In contrast to the Coulomb interaction $V_d(\mathbf{p}, \mathbf{p} + \mathbf{k}, \alpha, \alpha')$ which is local, i.e. not depending on \mathbf{p} , the exchange term $V_{\text{ex}}(\mathbf{p}, \mathbf{p} + \mathbf{k}, \alpha, \alpha')$, Eq. (C4), is non-local, depending on \mathbf{p} . It can be approximated by a local interaction after integration over p so that $\int d^3p V_{\text{ex}}(\mathbf{p}, \mathbf{p} + \mathbf{k}, \alpha, \alpha') = a_{\text{eff}}^2 Ze^2 \pi (28 + a_{\text{eff}}^2 k^2) / [\epsilon_0 \Omega (4 + a_{\text{eff}}^2 k^2)^4]$ results. This expression can be compared with the Pauli repulsion terms shown in the empirical pseudopotential, Eq. (17). In addition the these contributions V_d, V_{ex} , further terms are obtained from the expression (C2) containing the interaction with the core electron.

For an exploratory calculation, we can insert $V(\mathbf{p}, \mathbf{p} + \mathbf{k}, \alpha, \alpha') \approx V_d + V_{\text{ex}}$ in Eq. (18). Identifying a_{eff} with the parameter $r_1 = 0.17 \text{ \AA}$ the potential $\propto 1/(k^2 + \kappa^2) - 0.3/[(1 + 0.1p^2)(1 + 0.1(\mathbf{p} + \mathbf{k})^2)^{3/2}]$ (Rydberg units) reproduces well the static limit ($\omega \rightarrow 0$) of the collision frequency which is related to the dc conductivity. Whereas for the Debye potential V_d the real part of the dynamical collision frequency decreases with ω , see Fig. 5, the Pauli repulsion term together with the ionic structure factor gives at low temperatures a more constant value which goes down only at larger values of ω . For high temperatures, the effect of the Pauli repulsion term is reduced. Qualitatively, these findings correspond to the result shown in Fig. 10. The core electrons, in particular the Pauli blocking effects, have an important influence on the physical properties. A more detailed descriptions demands a systematic investigation of the interaction with the core electrons in complex systems such as aluminum, what is not intended in the present work.

-
- [1] R. P. Drake, *Phys. Plasmas* **16**, 055501 (2009).
- [2] J. J. Fortney, S. H. Glenzer, M. Koenig, B. Militzer, D. Saumon, and D. Valencia, *Phys. Plasmas* **16**, 041003 (2009).
- [3] B. A. Remington, *Plasma Phys. Control. Fusion* **47**, A191 (2005).
- [4] N. Nettelmann, A. Becker, and R. Redmer, *Astrophys. J.* **750**, 52 (2012).
- [5] N. Nettelmann, B. Holst, A. Kietzmann, M. French, R. Redmer, and D. Blaschke, *Astrophys. J.* **683**, 1217 (2008).
- [6] J. D. Lindl, P. Amendt, R. L. Berger, S. G. Glendinning, S. H. Glenzer, S. W. Haan, R. L. Kauffman, O. L. Landen, and L. J. Suter, *Phys. Plasmas* **11**, 339 (2004).
- [7] O. A. Hurricane, D. A. Callahan, D. T. Casey, P. M. Celliers, C. Cerjan, E. L. Dewald, T. R. Dittrich, T. Döppner, D. E. Hinkel, L. F. Berzak Hopkins, J. L. Kline, S. Le Pape, T. Ma, A. G. MacPhee, J. L. Milovich, A. Pak, H.-S. Park, P. K. Patel, B. A. Remington, J. D. Salmonson, P. T. Springer, and R. Tommasini, *Nature* **506**, 343 (2014).
- [8] J. Wicht, *Phys. Earth Planet. Int.* **132**, 281 (2002).
- [9] U. R. Christensen, V. Holzwarth, and A. Reiners, *Nature* **457**, 167 (2009).
- [10] U. R. Christensen, J. Aubert, and H. Gauthier, *Earth and Planet. Sci. Lett.* **296**, 487 (2010).
- [11] A. Aitta, *Icarus* **218**, 967 (2012).
- [12] T. Gastine, J. Wicht, L. D. V. Duarte, M. Heimpel, and A. Becker, *Geophys. Res. Lett.* **41**, 5410 (2014).
- [13] C. A. Jones, *Icarus* **241**, 148 (2014).
- [14] P. Olson, *Science* **342**, 431 (2013).
- [15] B. Hammel, S. Haan, D. Clark, M. Edwards, S. Langer, M. Marinak, M. Patel, J. Salmonson, and H. Scott, *High Energy Dens. Phys.* **6**, 171 (2010).
- [16] H. M. Milchberg, R. R. Freeman, S. C. Davey, and R. M. More, *Phys. Rev. Lett.* **61**, 2364 (1988).
- [17] A. N. Mostovych and Y. Chan, *Phys. Rev. Lett.* **79**, 5094 (1997).
- [18] Y. Ping, D. Hanson, I. Koslow, T. Ogitsu, D. Prendergast, E. Schwegler, G. Collins, and A. Ng, *Phys. Rev. Lett.* **96**, 255003 (2006).
- [19] S. Udea, N. Shilkin, V. E. Fortov, D. H. H. Hoffmann, J. Jacoby, M. I. Kulish, V. Mintsev, P. Ni, D. Nikolaev, N. A. Tahir, and D. Varentsov, *J. Phys. A: Math. Gen.* **39**, 4743 (2006).
- [20] T. Ao, Y. Ping, K. Widmann, D. F. Price, E. Lee, H. Tam, P. T. Springer, and N. A., *Phys. Rev. Lett.* **96**, 055001 (2006).
- [21] J. Clerouin, P. Noiret, V. Blottiau, B. Siberchicot, P. Renaudin, C. Blancard, G. Faussurier, B. Holst, and C. E. Starrett, *Phys. Plasmas* **19**, 082702 (2012).
- [22] M. W. C. Dharma-wardana and F. Perrot, *Phys. Lett. A* **163**, 223 (1992).
- [23] I. Krisch and H.-J. Kunze, *Phys. Rev. E* **58**, 6557 (1998).
- [24] A. W. DeSilva and J. D. Katsourous, *Phys. Rev. E* **57**, 5945 (1998).
- [25] Y. T. Lee and R. M. More, *Physics of Fluids* (1958-1988) **27**, 1273 (1984).
- [26] L. Spitzer and R. Härm, *Phys. Rev.* **89**, 977 (1953).
- [27] H. Reinholz, R. Redmer, G. Röpke, and A. Wierling, *Phys. Rev. E* **62**, 5648 (2000).
- [28] M. French, A. Becker, W. Lorenzen, N. Nettelmann, M. Bethkenhagen, J. Wicht, and R. Redmer, *Astrophys. J. Suppl. Ser.* **202**, 11 (2012).
- [29] M. Pozzo, C. Davies, D. Gubbins, and D. Alfé, *Nature* **485**, 355 (2012).
- [30] S. Kuhlbrodt, B. Holst, and R. Redmer, *Contrib. Plasma Phys.* **45**, 73 (2005).
- [31] K.-U. Plagemann, P. Sperling, R. Thiele, M. P. Desjarlais, C. Fortmann, T. Döppner, H. J. Lee, S. H. Glenzer, and R. Redmer, *New J. Phys.* **14**, 055020 (2012).
- [32] M. P. Desjarlais, J. D. Kress, and L. A. Collins, *Phys. Rev. E* **66**, 025401 (2002).
- [33] P. Emma, R. Akre, J. Arthur, R. Bionta, C. Bostedt, J. Bozek, A. Brachmann, P. Bucksbaum, R. Coffee, F. J. Decker, Y. Ding, D. Dowell, S. Edstrom, A. Fisher, J. Frisch, S. Gilevich, J. Hastings, G. Hays, Z. Hering, P. Huang, R. Iverson, H. Loos, M. Messerschmidt, A. Miahnahri, S. Moeller, H.-D. Nuhn, G. Pile, D. Ratner, J. Rzepiela, D. Schultz, T. Smith, P. Stefan, H. Tompkins, J. Turner, J. Welch, W. White, G. Yocky, and J. Galayda, *Nat. photonics* **4**, 641 (2010).
- [34] Y. Ding, A. Brachmann, F.-J. Decker, D. Dowell, P. Emma, J. Frisch, S. Gilevich, G. Hays, P. Hering, Z. Huang, R. Iverson, H. Loos, A. Miahnahri, H.-D. Nuhn, D. Ratner, J. Turner, J. Welch, W. White, and J. Wu, *Phys. Rev. Lett.* **102**, 254801 (2009).
- [35] P. Sperling, E. J. Gamboa, H. K. Chung, Y. Omarbakiyeva, H. Reinholz, G. Röpke, U. Zastrau, J. Hastings, L. B. Fletcher, S. H. Glenzer, and H.-J. Lee, *Phys. Rev. Lett.* **115**, 115001 (2015).
- [36] S. H. Glenzer and R. Redmer, *Rev. Mod. Phys.* **81**, 1625 (2009).
- [37] L. B. Fletcher, H. J. Lee, T. Döppner, E. Galtier, B. Nagler, P. Heimann, C. Fortmann, S. LePape, T. Ma, M. Millot, A. Pak, D. Turnbull, D. A. Chapmann, D. O. Gericke, J. Vorberger, T. White, G. Gregori, M. Wei, B. Barbrel, R. W. Falcone, C.-C. Kao, H. Nuhn, J. Welch, U. Zastrau, P. Neumayer, J. B. Hastings, and S. H. Glenzer, *Nat. Photonics* **9**, 274 (2015).
- [38] S. H. Glenzer, G. Gregori, R. W. Lee, F. J. Rogers, S. W. Pollaine, and O. L. Landen, *Phys. Rev. Lett.* **90**, 175002 (2003).
- [39] S. H. Glenzer, O. L. Landen, P. Neumayer, R. W. Lee, K. Widmann, S. W. Pollaine, R. J. Wallace, G. Gregori, A. Höll, T. Bornath, R. Thiele, V. Schwarz, W.-D. Kraeft, and R. Redmer, *Phys. Rev. Lett.* **98**, 065002 (2007).
- [40] E. G. Saiz, G. Gregori, D. O. Gericke, J. Vorberger, B. Barbrel, R. J. Clarke, R. R. Freeman, S. H. Glenzer, F. Y. Khattak, M. Koenig, O. L. Landen, D. Neely, P. Neumayer, M. M. Notley, A. Pelka, D. Price, M. Roth, M. Schollmeier, C. Spindloe, R. L. Weber, L. van Woerkom, K. Wünsch, and D. Riley, *Nat. Phys.* **4**, 940 (2008).
- [41] A. L. Kritcher, P. Neumayer, J. Castor, T. Döppner, R. W. Falcone, O. L. Landen, H. J. Lee, R. W. Lee, E. C. Morse, A. Ng, S. Pollaine, D. Price, and S. H. Glenzer, *Science* **322**, 69 (2008).
- [42] U. Zastrau, P. Sperling, M. Harmand, A. Becker, T. Bornath, R. Bredow, S. Dziarzhytski, T. Fennel, L. Fletcher, E. Förster, S. Göde, G. Gregori, V. Hilbert, D. Hochhaus,

- B. Holst, T. Laarmann, H. J. Lee, T. Ma, J. P. Mithen, R. Mitzner, C. Murphy, M. Nakatsutsumi, P. Neumayer, A. Przystawik, S. Roling, M. Schulz, B. Siemer, S. Skruszewicz, R. Thiele, J. Tiggesbäumker, S. Toleikis, T. Tschentscher, T. White, M. Wöstmann, H. Zacharias, T. Döppner, S. H. Glenzer, and R. Redmer, *Phys. Rev. Lett.* **112**, 105002 (2014).
- [43] B. Lengeler, C. G. Schroer, M. Kuhlmann, B. Benner, T. F. Günzler, O. Kurapova, F. Zontone, A. Snigirev, and I. Snigireva, *Journal of Physics D: Applied Physics* **38**, A218 (2005).
- [44] R. Fäustlin, T. Bornath, T. Döppner, S. Düsterer, E. Förster, C. Fortmann, S. H. Glenzer, S. Göde, G. Gregori, R. Irsig, T. Laarmann, H. Lee, B. Li, K.-H. Meiwes-Broer, J. Mithen, B. Nagler, A. Przystawik, H. Redlin, R. Redmer, H. Reinholz, G. Röpke, F. Tavella, R. Thiele, J. Tiggesbäumker, S. Toleikis, I. Uschmann, S. Vinko, T. Whitcher, U. Zastrau, B. Ziaja, and T. Tschentscher, *Phys. Rev. Lett.* **104**, 125002 (2010).
- [45] U. Zastrau, A. Woldegeorgis, E. Förster, R. Loetzsch, H. Marschner, and I. Uschmann, *J. Instrum.* **8**, P10006 (2013).
- [46] U. Zastrau, L. B. Fletcher, E. Förster, E. C. Galtier, E. J. Gamboa, S. H. Glenzer, P. Heimann, H. Marschner, B. Nagler, A. Schropp, O. Wehrhan, and H. J. Lee, *Rev. Sci. Instr.* **85**, 093106 (2014).
- [47] L. B. Fletcher, E. Galtier, P. Heimann, H.-J. Lee, B. Nagler, J. Welch, U. Zastrau, J. Hastings, and S. Glenzer, *J. Instrum.* **8**, C11014 (2013).
- [48] G. Gregori, S. H. Glenzer, H.-K. Chung, D. Froula, R. Lee, N. Meezan, J. Moody, C. Niemann, O. Landen, B. Holst, R. Redmer, S. Regan, and H. Sawada, *J. Quant. Spectrosc. Radiat. Transfer* **99**, 225 (2006).
- [49] H.-K. Chung, M. H. Chen, and R. W. Lee, *High Energy Dens. Phys.* **3**, 57 (2007).
- [50] J. C. Stewart and K. D. Pyatt, *Astrophys. J.* **144**, 1203 (1966).
- [51] D. S. Rackstraw, S. M. Vinko, O. Ciricosta, B. I. Cho, K. Engelhorn, H.-K. Chung, C. R. D. Brown, T. Burian, J. Chalupský, C. Falcone, R. W. Graves, V. Hjkov, A. Higginbotham, L. Juha, J. Krzywinski, H. J. Lee, M. Messerschmidt, C. Murphy, Y. Ping, A. Scherz, W. Schlotter, S. Toleikis, J. Turner, L. Vysin, T. Wang, B. Wu, U. Zastrau, D. Zhu, B. Nagler, R. W. Lee, P. A. Heimann, and J. S. Wark, *High Energy Dens. Phys.* **11**, 59 (2014).
- [52] N. Medvedev, U. Zastrau, E. Förster, D. O. Gericke, and B. Rethfeld, *Phys. Rev. Lett.* **107**, 165003 (2011).
- [53] A. Höll, T. Bornath, L. Cao, T. Döppner, S. Düsterer, E. Förster, C. Fortmann, S. H. Glenzer, G. Gregori, T. Laarmann, K.-H. Meiwes-Broer, A. Przystawik, P. Radcliffe, R. Redmer, H. Reinholz, G. Röpke, R. Thiele, J. Tiggesbäumker, J. Toleikis, N. X. Truong, T. Tschentscher, I. Uschmann, and U. Zastrau, *High Energy Dens. Phys.* **3**, 120 (2007).
- [54] J. Chihara, *J. Phys. F* **17**, 295 (1987).
- [55] J. Chihara, *J. Phys. Cond. Matter* **12**, 231 (2000).
- [56] N. D. Mermin, *Phys. Rev. B* **1**, 2362 (1970).
- [57] G. Röpke, A. Selchow, A. Wierling, and H. Reinholz, *Phys. Lett. A* **260**, 365 (1999).
- [58] G. Röpke, *Phys. Rev. E* **57**, 4673 (1998).
- [59] A. Wierling, T. Millat, G. Röpke, R. Redmer, and H. Reinholz, *Phys. Plasmas* **8**, 3810 (2001).
- [60] P. Neumayer, C. Fortmann, T. Döppner, P. Davis, R. W. Falcone, A. L. Kritcher, O. L. Landen, H. J. Lee, R. W. Lee, C. Niemann, S. Le Pape, and S. H. Glenzer, *Phys. Rev. Lett.* **105**, 075003 (2010).
- [61] G. R. Gathers, *Int. J. Thermophys.* **4**, 209 (1983).
- [62] P. D. Desai, H. M. James, and C. Y. Ho, *J. Phys. Chem. Ref. Data* **13**, 1131 (1984).
- [63] G. Faussurier and C. Blancard, *Phys. Rev. E* **91**, 013105 (2015).
- [64] M. W. C. Dharma-wardana, arXiv , 1601.07566 (2016).
- [65] M. R. Zaghloul, M. A. Bourham, and J. M. Doster, *J. Phys. D: Appl. Phys.* **33**, 977 (2000).
- [66] C. Blancard and G. Faussurier, *Phys. Rev. E* **69**, 016409 (2004).
- [67] A. Ng, P. Celliers, A. Forsman, R. M. More, Y. T. Lee, F. Perrot, M. W. C. Dharma-wardana, and G. A. Rinker, *Phys. Rev. Lett.* **72**, 3351 (1994).
- [68] N. W. Ashcroft and J. Lekner, *Phys. Rev.* **145**, 83 (1966).
- [69] T. Schneider and E. Stoll, *Phys. kondens. Materie* **5**, 331 (1966).
- [70] G. Röpke, *Phys. Rev. A* **38**, 3001 (1988).
- [71] H. Reinholz, G. Röpke, S. Rosmej, and R. Redmer, *Phys. Rev. E* **91**, 043105 (2015).
- [72] J. M. Ziman, *Philos. Mag.* **6**, 1013 (1961).
- [73] Y. Waseda, *The Structure of Non-Crystalline Materials, Liquids and* (McGraw-Hill, New York, 1980).
- [74] J. M. Stallard and C. Davis Jr., *Phys. Rev. A* **8**, 368 (1973).
- [75] M. S. Wertheim, *Phys. Rev. Lett.* **10**, 321 (1963).
- [76] R. Bredow, T. Bornath, W.-D. Kraeft, M. W. C. Dharma-wardana, and R. Redmer, *Contrib. Plasma Phys.* **55**, 222 (2015).
- [77] R. Bredow, , private communication (2015).
- [78] T. E. Faber, *Introduction of the Theory of Liquid Metals* (Cambridge University Press, Cambridge, England, 1972).
- [79] R. Reinholz and G. Röpke, *Phys. Rev. E* **85**, 036401 (2012).